

Estimating Dispersion Curves from Frequency Response Functions via Vector-Fitting

Mohammad I. Albakri^{a,1,*}, Vijaya V. N. Sriram Malladi^{b,1}, Serkan Gugercin^d, Pablo A. Tarazaga^c

^aDepartment of Mechanical Engineering, Tennessee Technological University

^bDepartment of Mechanical Engineering - Engineering Mechanics, Michigan Technological University

^cDepartment of Mechanical Engineering, Virginia Polytechnic Institute and State University

^dDepartment of Mathematics, Virginia Polytechnic Institute and State University

Abstract

Driven by the need for describing and understanding wave propagation in structural materials and components, several analytical, numerical, and experimental techniques have been developed to obtain dispersion curves. Accurate characterization of the structure (waveguide) under test is needed for analytical and numerical approaches. Experimental approaches, on the other hand, rely on analyzing waveforms as they propagate along the structure. Material inhomogeneity, reflections from boundaries, and the physical dimensions of the structure under test limit the frequency range over which dispersion curves can be measured.

In this work, a new data-driven modeling approach for estimating dispersion curves is developed. This approach utilizes the relatively easy-to-measure, steady-state Frequency Response Functions (FRFs) to develop a state-space dynamical model of the structure under test. The developed model is then used to study the transient response of the structure and estimate its dispersion curves. This paper lays down the foundation of this approach and demonstrates its capabilities on a one-dimensional homogeneous beam using numerically calculated FRFs. Both in-plane and out-of-plane FRFs corresponding, respectively, to longitudinal (the first symmetric) and flexural (the first anti-symmetric) wave modes are analyzed. The effects of boundary conditions on the performance of this approach are also addressed.

Keywords: data driven modeling, dispersion curves, vector fitting, spectral element method, wave propagation

1. Introduction

Understanding wave propagation in structures is essential for numerous applications such as structural health monitoring, material characterization, stress-state identification [1], event detection and localization [2–4], vibration suppression, and elastic meta-structures [5]. Key to this understanding is the ability to describe the frequency-dependent nature of wave propagation characteristics governed by dispersion curves. Dispersion relations of elastic waves are determined by geometric and material characteristics of the waveguide, as well as the nature of the deformations induced by the propagating wave (the wave mode) [6].

Analytical models have been developed to derive dispersion relations for numerous materials and waveguides [6]. For commonly used homogeneous and heterogeneous materials, dispersion relations

*Address all correspondence to this author. Email: malbakri@vt.edu

¹These authors have contributed equally

have been documented in various handbooks and textbooks [7, 8]. Numerical methods, such as time and frequency domain spectral element method [9–12], the semi-analytical finite element method [13, 14], the wave finite element method [15, 16], and transfer function and transfer matrix methods [17, 18] have also been developed to describe wave propagation along uniform and periodically varying waveguides. For realistic wave propagation characteristics to be obtained, accurate description of material and geometric characteristics of the waveguide is required [19]. Accurate characterization of waveguides can be challenging, especially when inhomogeneous materials, such as wood and steel-reinforced concrete, and unconventional structures, such as 3D printed and smart structures with integrated sensors and actuators, are being considered. Experimental methods for measuring dispersion relations have also been developed where a tone burst is induced in the structure under test and then analyzed as it propagates along the structure. However, material inhomogeneity, complex boundary conditions, and the physical dimensions of the structure under test pose challenges to such techniques. In particular, the ability of current techniques to measure the low frequency portions of dispersion curves, which are very important for event localization and stress-state identification applications, is limited by structure’s dimensions, damping, and reflections from structure’s boundaries.

Data-driven modeling provides an alternative approach to create numerical models that capture the dynamic response of the structure under test. Such models rely completely on measured responses, thus, any knowledge of the underlying physical characteristics of the structure is not required. In this context, the data amounts to a large set of frequency response measurements and the modeling amounts to constructing a low-dimensional rational function to fit this data in an appropriate sense. This is a heavily studied topic with varying approaches based on the eventual goal; see, e.g., [20–23] for rational approximations that enforce interpolation of the measured data; [24–28] for rational approximations that minimize a least-squares deviation from the measured data; and [29, 30] for rational approximations that combine the interpolation and least-squares formulation. Here, the least-squares based Vector Fitting [26] framework will be employed.

In this work, a new data-driven approach for estimating dispersion curves is developed. Steady-state dynamic responses, in the form of Frequency Response Functions (FRFs), are used to build the data-driven model of the structure under consideration. The developed model is then used to simulate the transient dynamic response of the structure which, in turn, is analyzed to reconstruct dispersion curves. The capabilities of this approach are demonstrated on a simple one-dimensional structure for which exact dispersion curves are attainable. The work builds on a previous effort by the authors [31] and discusses in detail the development of this approach using numerical experiments. The applicability of this approach to symmetric (longitudinal) and anti-symmetric (flexural) wave modes is investigated. These wave modes are selected as they are the simplest to analyze theoretically and experimentally. Other wave modes along with wave propagation in two-dimensional structures, such as plates, will be addressed in future studies. This new approach is proposed as an alternative to the traditional experimental techniques, with the potential of overcoming the aforementioned limitations, especially when low-frequency portions of the dispersion curves are of interest. Furthermore, the fact that the developed approach relies on the steady-state dynamic response to estimate dispersion curves, as opposed to transient waveform measurements, relaxes sampling rate requirements and improves signal-to-noise ratio in testing.

This paper is structured as follows: Section 2 briefly presents the development of the numerical model used to generate the FRFs to construct data-driven models. Elementary rod and Timoshenko beam approximate theories, along with the frequency domain spectral element method, are used to develop this model, which also provides the exact dispersion curves for comparison. Data-driven rational approximation is discussed in Section 3 where the simulated FRFs are used to build a data-driven, state-space model that describes the dynamics of the beam under test. The layout of the newly developed approach is discussed in Section 4 where dispersion curves of the first anti-symmetric wave mode are estimated. The

applicability of this approach to estimate dispersion relations for symmetric wave modes are presented in Section 5. Section 6 discusses the effects of boundary conditions on the performance of this approach. Finally, concluding remarks are presented in Section 7.

2. Mathematical Model and Spectral Element Formulation

Consider a long beam excited with a pair of identical piezoelectric actuators, as shown in Figure 1. The piezoelectric actuators can be excited either in-phase to generate pure longitudinal deformations or out-of-phase for pure flexural excitation. This excitation configuration is selected here since it is commonly used in experimental studies. Due to the structure symmetry around its neutral axis, longitudinal and flexural deformations are completely uncoupled. For simplicity, the piezoelectric actuators are replaced with two pairs of longitudinal forces acting at the beam's upper and lower surfaces, as shown in Figure 1. Readers are referred to [32, 33] for detailed formulation of piezoelectric-augmented structures.

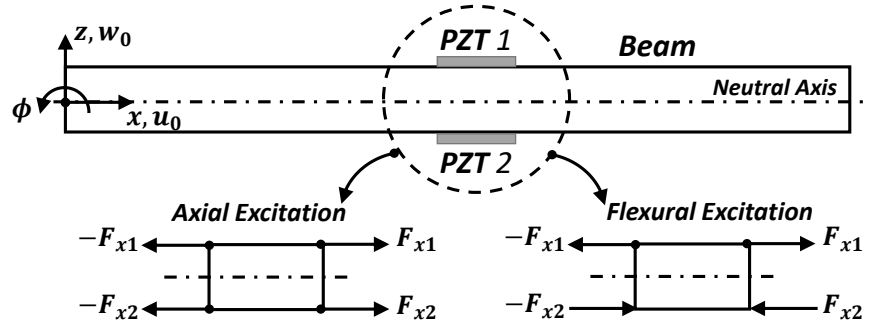


Figure 1: Schematic of a beam excited with surface mounted piezoelectric actuators (PZT).

The mass and stiffness of the piezoelectric actuators are assumed to be negligible compared to those of the beam. Following the Elementary rod and the Timoshenko beam approximate theories, the elastodynamic equations of motion can be expressed as

$$\begin{aligned} \rho A \frac{\partial^2 u_0}{\partial t^2} - \frac{\partial u_0}{\partial x} \left(EA \frac{\partial u_0}{\partial x} \right) &= qA, \\ \rho A \frac{\partial^2 w_0}{\partial t^2} - GA\bar{K} \frac{\partial}{\partial x} \left(\frac{\partial w_0}{\partial x} - \phi \right) &= P, \\ \rho I \frac{\partial^2 \phi}{\partial t^2} - EI \frac{\partial^2 \phi}{\partial x^2} - GA\bar{K} \left(\frac{\partial w_0}{\partial x} - \phi \right) &= 0, \end{aligned} \quad (1)$$

with the boundary conditions

$$EA \frac{\partial u_0}{\partial x} = F_x, \quad GA\bar{K} \left(\frac{\partial w_0}{\partial x} - \phi \right) = F_z, \quad \text{and} \quad EI \frac{\partial \phi}{\partial x} = M, \quad (2)$$

where u_0 and w_0 denote the longitudinal and lateral displacements of the beam's neutral axis, respectively; ϕ denotes the angle of rotation of the neutral axis normal vector; ρ , E , and G are, respectively, the material's volumetric mass density, elasticity modulus, and rigidity modulus; A is the beam's cross sectional area; and I is its second moment of area. The Timoshenko correction factor, \bar{K} , is determined by matching the high-frequency wave speed to that of Rayleigh waves [9]. $q(x, t)$ is the externally applied

axial body force per unit volume and $P(x, t)$ is the externally applied transverse distributed load. Both q and P are non-existent in the current analysis. The externally applied concentrated longitudinal forces, lateral forces, and bending moments are denoted by F_x , F_z , and M , respectively.

The frequency domain Spectral Element Method (SEM) is used to solve the elastodynamic equations of motion and to obtain FRFs corresponding to longitudinal and flexural deformations. This method is selected over other numerical methods, such as the FEM, due to its superior accuracy [11]. This is especially important when the high-frequency dynamic response is of interest. The spectral element formulation is briefly presented in this section.

With the SEM, all variables appearing in the equations of motion, along with boundary conditions, are first transformed to frequency domain using the discrete Fourier transform, and a spectral solution of the following form is assumed

$$\mathbf{u}(x, t) = \frac{1}{\hat{N}} \sum_{n=0}^{\hat{N}-1} \sum_{m=1}^M r_{lm} A_m e^{-i(k_{mn}x - \omega_n t)}, \quad (3)$$

where $\mathbf{u}(x, t) = [u_0(x, t) \ w_0(x, t) \ \phi(x, t)]^T$ is the response variables vector in time domain; \hat{N} is the number of spectral components considered in the discrete Fourier transform, M is the number of wave-modes contributing to the displacement-field, k_{mn} is the wave number corresponding to the m^{th} mode at the n^{th} angular frequency (ω_n), and $i = \sqrt{-1}$. Fourier coefficients at ω_n are represented in terms of the scaling matrix, \mathbf{r} , and the amplitude vector \mathbf{A} . The variable l takes the value of 1, 2, or 3 for u_0 , w_0 , and ϕ , respectively.

Fourier coefficients corresponding to the coupled variables, w_0 and ϕ , can be scaled relative to either one of them. In this work, the coefficient corresponding to w_0 is chosen to be the scaling coefficient, hence, $r_{2m} = 1, \forall m$. The uncoupled axial deformations u_0 , on the other hand, can be solved for independently. Thus, no scaling factor is required for this component.

Substituting the spectral solution, (3) into the governing equations (1) yields

$$\begin{aligned} & \left(-\rho\omega_n^2 + Ek_{mn}^2 \right) A_m = 0, \\ & \begin{bmatrix} GA\bar{K}k_{mn}^2 - \rho A\omega_n^2 & -iGA\bar{K}k_{mn} \\ iGA\bar{K}k_{mn} & EI k_{mn}^2 - \rho I\omega_n^2 + GA\bar{K} \end{bmatrix} \begin{bmatrix} 1 \\ r_{3m} \end{bmatrix} A_m = 0, \end{aligned} \quad (4)$$

For each frequency of interest, ω_n , the characteristic equations are solved for the wavenumber k_{mn} , which results in three wavemodes. These wavemodes represent the propagating first symmetric and first anti-symmetric modes, along with the evanescent second anti-symmetric mode. The later wavemode transfers to propagating upon passing through the cut-off frequency $\omega_c = \sqrt{GA\bar{K}/\rho I}$. Group velocity for each propagating mode is then calculated as $V_{Gm} = \partial\omega_n/\partial k_{mn}$. These results are used in later sections to assess the performance of the data-driven approach. Once the characteristic equations are solved, the scaling constants, r_{3m} , are calculated for each mode m .

To calculate FRFs corresponding to longitudinal and flexural deformations of the structure, the dynamic stiffness matrix, $\mathbf{K}(i\omega)$ is first evaluated. This matrix relates the nodal displacements vector, \mathbf{d} , and the nodal forces and moments vector, \mathbf{F} , in the frequency domain. The dynamic stiffness matrix is defined in terms of the shape functions matrix, $\mathbf{\Psi}(i\omega)$, and the boundary conditions matrix, $\mathbf{G}(i\omega)$, as follows

$$\mathbf{F} = \mathbf{K}(i\omega)\mathbf{d} = \mathbf{\Psi}(i\omega)^{-1}\mathbf{G}(i\omega)\mathbf{d}, \quad (5)$$

where \mathbf{d} , \mathbf{F} , $\mathbf{\Psi}$, and \mathbf{G} for a two-node spectral finite element are defined in Appendix A.

Although spatial discretization is not required for uniform, homogeneous structures, three spectral finite elements are used for the current analysis. This is done to allow the application of the desired excitation configuration described in Figure 1. Standard assembly procedures are applied to obtain the global dynamic stiffness matrix.

The beam considered here is a 48-in. long rectangular beam, with a $1 \times 1/8$ -in.² cross sectional area. The beam is made of Aluminum, with $E = 69 \text{ GPa}$, $G = 26 \text{ GPa}$ and $\rho = 2700 \text{ kg/m}^3$. Piezoelectric wafers are bonded to the beam's upper and lower surfaces, 18.5 in. from its left end. A total of 23 receptance FRFs are calculated. These are the driving-point FRF (calculated at the right edge of the piezoelectric actuator) along with 22 transfer FRFs calculated over a span of 22 in., with 1-in. increments. FRFs are calculated over the frequency range of 0 to 50 kHz with 0.25 Hz resolution. Several boundary conditions are investigated in this study. The analysis is first presented for the free-free case. Other boundary conditions are discussed in Section 6.

3. Data-driven Rational Approximation

This section briefly outlines the mathematical framework employed to construct rational approximations (state-space models) from a given set of FRF measurements. To make the notation more clear and the discussion more concise, the methodology for only scalar measurements is presented, i.e., it is assumed that FRF measurements come from a single-input single-output dynamical system. Theory and numerical implementations are already established for multi-input multi-output systems, and the reader is referred to [26, 34] for those details.

Let $\mathcal{H}(i\omega) \in \mathbb{C}$ denote the FRF of the underlying dynamics evaluated at the frequency ω . Then, the starting point is a set of FRF samples at selected frequencies, denoted by $\{\mathcal{H}(i\omega_1), \mathcal{H}(i\omega_2), \dots, \mathcal{H}(i\omega_N)\}$ where N is a positive integer. In this paper where the theoretical framework is established, these FRFs are obtained by sampling the analytical transfer functions derived from Eq. (5). More specifically, the components of the inverse of the dynamic-stiffness matrix, i.e., $\mathbf{K}^{-1}(i\omega)$, corresponding to the out-of-plane and in-plane displacements are sampled over the frequency range of interest. In practice, these samples will be obtained via experimental measurements.

Given the samples, $\{\mathcal{H}(i\omega_j)\}$ for $j = 1, 2, \dots, N$, the goal is, now, to construct a degree- r dynamical system described by its degree- r rational function (FRF), $\tilde{\mathcal{H}}(s) = \tilde{\mathbf{C}}(s\mathbf{I} - \tilde{\mathbf{A}})^{-1}\tilde{\mathbf{B}}$, that fits the data in an appropriate sense. The degree- r means that $\tilde{\mathbf{A}} \in \mathbb{R}^{r \times r}$, $\tilde{\mathbf{B}} \in \mathbb{R}^{r \times 1}$, and $\tilde{\mathbf{C}} \in \mathbb{R}^{1 \times r}$. In this work, the least-squares (LS) measure is used to judge the quality of the data-driven model:

$$\text{Find the degree-}r \text{ rational function } \tilde{\mathcal{H}}(s) \text{ that minimizes } \sum_{j=1}^N \left| \mathcal{H}(i\omega_j) - \tilde{\mathcal{H}}(i\omega_j) \right|^2. \quad (6)$$

The Vector Fitting (VF) method of Gustavsen et al. [26] is used (and adopted to our setting) in solving the LS problem (6). This approach is briefly explained in this section.

Let $n(s) = \alpha_0 + \alpha_1 s + \dots + \alpha_{r-1} s^{r-1}$ and $d(s) = \beta_0 + \beta_1 s + \dots + \beta_{r-1} s^{r-1} + s^r$ denote, respectively, the numerator and denominator of the degree- r rational function $\tilde{\mathcal{H}}(s)$, i.e.,

$$\tilde{\mathcal{H}}(s) = \frac{n(s)}{d(s)} = \frac{\alpha_0 + \alpha_1 s + \dots + \alpha_{r-1} s^{r-1}}{\beta_0 + \beta_1 s + \dots + \beta_{r-1} s^{r-1} + s^r}.$$

The numerator $n(s)$ has degree- $r - 1$ (as opposed to degree- r) since $\mathcal{H}(s)$ does not have a direct feed through term; thus, it is a strictly proper rational function. The formulation can be easily modified

to allow a degree- r numerator; but for the problems presented herein, $\mathcal{H}(s)$ is strictly proper. Now notice that the unknowns appear both in $n(s)$ and $d(s)$; thus the minimization problem (6) is a *nonlinear* LS problem and cannot be solved with direct methods in one step, as is the case for linear LS problems. An iterative scheme is needed: the nonlinear LS problem (6) is solved iteratively by solving a sequence of linear LS problems. This is achieved by linearizing the error function $\mathcal{H}(s) - \tilde{\mathcal{H}}(s)$. Using $\tilde{\mathcal{H}}(s) = \frac{n(s)}{d(s)}$, the LS error in (6) can be rewritten as

$$\sum_{j=1}^N \left| \mathcal{H}(i\omega_j) - \tilde{\mathcal{H}}(i\omega_j) \right|^2 = \sum_{j=1}^N \frac{|d(i\omega_j)\mathcal{H}(i\omega_j) - n(i\omega_j)|^2}{|d(i\omega_j)|^2}, \quad (7)$$

which is still nonlinear in the variables. Starting with the $d^{(0)}(s) \equiv 1$, Sanathanan and Koerner [35] proposed an iterative scheme where at the k^{th} step

$$\text{the LS error } \sum_{i=1}^N \left| \frac{n^{(k+1)}(\xi_i) - d^{(k+1)}(\xi_i)\mathcal{H}(\xi_i)}{d^{(k)}(\xi_i)} \right|^2 \text{ is minimized by solving for } n^{(k+1)}(s) \text{ and } d^{(k+1)}(s). \quad (8)$$

Note the difference from the earlier problem. The relaxed LS problem in (8) is linear in the variables $n^{(k+1)}(s)$ and $d^{(k+1)}(s)$, and can be solved using linear LS solution techniques. Then, the process is repeated using the new denominator $d^{(k+1)}(s)$ until convergence is achieved. This is the SK iteration to solve the original nonlinear LS problem (6).

The VF method is a further improvement on the SK iteration and uses a different parameterization for $\tilde{\mathcal{H}}(s)$; specifically, VF uses the barycentric-form for a rational function: At the k^{th} step of the VF iteration, the approximation is parameterized as

$$\tilde{\mathcal{H}}^{(k)}(s) = \frac{\tilde{n}^{(k)}(s)}{\tilde{d}^{(k)}(s)} = \frac{\sum_{j=1}^r \phi_j^{(k)} / (s - \lambda_j^{(k)})}{1 + \sum_{j=1}^r \psi_j^{(k)} / (s - \lambda_j^{(k)})}, \quad \text{where } \phi_j^{(k)}, \psi_j^{(k)}, \lambda_j^{(k)} \in \mathbb{C}. \quad (9)$$

The advantage of this formulation is that the *poles* $\lambda_j^{(k)}$ are an arbitrary set of mutually distinct points. Note that $\lambda_j^{(k)}$ are *not* the poles of $\tilde{\mathcal{H}}^{(k)}(s)$ unless $\psi_j^{(k)} = 0$ for $j = 1, 2, \dots, r$. As in the SK iteration, for fixed poles $\lambda_j^{(k)}$, the LS problem for $\tilde{\mathcal{H}}^{(k)}(s)$ in (9) becomes linear in the remaining variables $\phi_j^{(k)}$ and $\psi_j^{(k)}$. Then, the VF algorithm continues the iteration by updating the poles $\lambda_j^{(k)}$ as the zeros of the numerator in Eq. (9), i.e., as the zeroes of $\tilde{d}^{(k)}(s) = 1 + \sum_{j=1}^r \psi_j^{(k)} / (s - \lambda_j^{(k)})$. This iteration is run until convergence of the poles $\lambda_j^{(k)}$, upon which the denominator $\tilde{d}^{(k)}(s) \rightarrow 1$ and the final rational approximant is given by

$$\tilde{\mathcal{H}}(s) = \sum_{j=1}^r \frac{\phi_j}{s - \lambda_j} = \tilde{\mathbf{C}}(s\mathbf{I} - \tilde{\mathbf{A}})^{-1}\tilde{\mathbf{B}}. \quad (10)$$

For further details, we refer the reader to [26, 36]. VF has successfully been used in many applications and various modifications have been proposed. The pole relocation step has been improved [37], the MIMO case has been efficiently parallelized [38], it has been combined with quadrature-based sampling [27], and it has been analyzed in detail in terms of numerical robustness [34]. The reader is referred to [28] where a rational Krylov toolbox has been developed to solve similar nonlinear LS problems. The Loewner framework, introduced by Mayo and Antoulas [22], is another commonly used approach to construct rational approximants from FRF measurements. In this case, the approximant is sought to be an (approximant) interpolant as opposed to a LS fit. The recently developed Adaptive Anderson-Antoulas

algorithm [29] is a hybrid approach where a rational interpolant is constructed to interpolate a subset of the data and to minimize LS error in the rest. As pointed out earlier, in this work, the focus is on the LS framework where the regular VF framework is used to solve the data-driven modeling problem.

4. Data-driven Model based Dispersion Curves for Flexural Waves

The proposed approach for estimating dispersion curves utilizes FRFs to generate a single-input multi-output (SIMO), data-driven, state-space model, $\tilde{\mathcal{H}}(s)$, of the structure under consideration. This model is then used to simulate the transient dynamic response of the structure to a given excitation. Simulated responses are then analyzed in the frequency domain to reconstruct dispersion curves. The analysis is first presented for out-of-plane (flexural) receptance FRFs, corresponding to the first anti-symmetric wave mode. The analysis is repeated for the first symmetric wave mode, using the in-plane (longitudinal) FRFs, in Section 5. The process of estimating dispersion curves from FRFs can be split into two main stages: (i) the development of the data-driven model using VF and (ii) transient response simulation and analysis. The two stages are discussed in detail in the following subsections.

4.1. Data-driven Modeling using VF

In this section, a SIMO, data-driven, state-space model, $\tilde{\mathcal{H}}(s)$, is developed based on the simulated FRFs for the beam over the frequency range of 0.01 to 50 kHz. FRFs are sampled such that the frequency resolution is 0.25 Hz over the entire frequency range of 50 kHz. Such fine frequency resolution is needed to better capture lower-order resonant frequencies, resulting in approximately 200,000 samples. As discussed in detail below, an accurate $\tilde{\mathcal{H}}(s)$ for the full frequency spectrum requires an approximation order of $r > 200$. Since we are measuring 23 FRFs, this means that every VF iteration requires solving a linear least-squares problem with a dense coefficient matrix having more than 2.5×10^6 rows and 4800 columns. Since the coefficient matrix changes at every step, this is not a trivial numerical task and needs careful numerical implementation such as those in [34, 38].

However, the main issue in trying to fit the FRFs directly on the full frequency spectrum is the sensitivity to the initial pole selection. As discussed in Section 3, the VF algorithm is initialized by a set of poles. While for modest r values and for a smaller number of measurements, the VF algorithm does a good job of correcting the poles during the iteration, for the scale of the problems and for the complex dynamics considered here, a not-well-informed initial pole selection leads to inaccurate rational approximants together with potentially highly ill-conditioned least-squares problems to solve; in other words, for the setting considered in this paper, the quality of the fitted model is more dependent on the choice of starting poles; see [26, 28, 37] for related work. Moreover, when experimentally measured noisy FRFs are used, these issues will be further magnified. Therefore, in order to develop a framework that is much better suited for experimentally collected data, a more comprehensive initialization procedure is developed for VF. For this purpose, the full frequency range is divided into multiple smaller bands. Since high-quality rational approximations in smaller frequency bands can be obtained via smaller approximation orders, for each frequency band, the initial, but now much smaller number of poles for VF, are selected by taking into account the quantity and the location of resonant frequencies. Additionally, due to the free-free boundary conditions, rigid-body modes appear in the FRFs at 0 Hz. While the VF algorithm can handle fitting these modes, numerical instabilities arising from the 0 Hz pole renders simulation results inaccurate. To avoid such numerical instabilities, rigid-body modes are eliminated in the current analysis.

Once these smaller frequency bands are fitted, the resulting poles are put together to initialize the VF algorithm for the entire frequency range. With this much improved initial pole selection, VF converges quickly for the whole frequency range and yields an accurate rational approximation, as illustrated in the numerical examples below. The following steps further discuss the details of this process.

Step 1: VF of FRF Partitioned into Multiple Bands

Since for dispersive media, such as beams and plates, the frequency spacing between resonant frequencies is not uniform, random assignment of initial poles would not be practical. For instance, in 1-dimensional dispersive structures, the frequency spacing between consecutive natural frequencies increases with mode number. As a result, modal density is higher at lower frequency ranges, i.e., there are more resonant peaks in the 0 – 1 *kHz* range than, for example, the 2 – 3 *kHz* range. This becomes even more important when dealing with noisy experimental data. As a result, the VF algorithm is initialized using poles that are obtained by fitting FRFs over smaller frequency bands.

When fitting out-of-plane FRFs, the full frequency range is divided into smaller bands in order to achieve high-quality rational approximations. Seven frequency bands, with comparable modal density, were selected for this purpose. Details of the number of resonant peaks and the corresponding number of poles used to fit FRF in each band is tabulated in Table 1. Each resonant peak of the FRF is represented by a pair of complex-conjugate poles, where the n^{th} pair of poles are of the form $p^{2n-1} = \alpha + i\beta$, $p^{2n} = \alpha - i\beta$. Therefore, the number of poles of the fitted model are at least twice the number of resonant frequencies in the frequency band of interest. While the imaginary part (β) of these poles indicates the oscillatory behavior, the real part (α) represents the damping characteristic of the dynamical system. Resonant peak frequencies are used as the initial values for β , whereas the real part is initialized as $\alpha = \beta/100$, following the recommendation of [26]. The effect of initial pole placement and model order on the performance of this approach will be further investigated in future studies. Table 1 summarizes fitting results for each frequency band. The quality of the fit is determined using a relative L_2 error defined as

$$\mathcal{E}_{L_2}^{rel} = \frac{1}{N} \sqrt{\frac{\sum_{i=1}^N \|\mathcal{H}(i\omega_i) - \tilde{\mathcal{H}}(i\omega_i)\|_F^2}{\sum_{i=1}^N \|\mathcal{H}(i\omega_i)\|_F^2}}. \quad (11)$$

where $\|\cdot\|_F$ denotes the Frobenious norm. Table 1 demonstrates that the constructed models fit the data to a high relative accuracy.

While the minimum number of poles required to fit each frequency band is twice the number of resonant peaks in that band, adding extra poles to account for near by resonant peaks, that have strong influence on the FRFs in that band, was found to be necessary. For example, at least 28 complex poles were needed to fit the FRF within the frequency band of 0 - 1 *kHz*, which only has 13 resonant peaks. A closer examination of the fitted poles shows that the two additional poles correspond to a resonant peak at 1038 *Hz*, which is very close to the current frequency band of interest. Table 1 shows the number of resonant peaks in each frequency band along with the number of poles needed to fit FRFs over each band.

Step 2: VF of the Entire FRF

Once the poles of the state-space models for each frequency band are determined, they are combined together to initialize VF over the entire frequency range. While combining these poles, it is important to avoid duplicating them. The complete FRF with 106 resonant peaks is fitted with 212 poles, exactly the minimum number of poles required to fit all resonant peaks over this frequency range. The result is a data-driven, state-space model of the form:

$$\tilde{\mathcal{H}}(s) = \tilde{\mathbf{C}}(s\mathbf{I} - \tilde{\mathbf{A}})^{-1}\tilde{\mathbf{B}}, \quad (12)$$

Table 1: Number of resonant peaks and initial poles in partitioned frequency bands

Band	Frequency range	Resonant peaks	No. of poles	$\mathcal{E}_{L_2}^{rel}$
1	0.01 - 1kHz	13	28	1.02×10^{-5}
2	1 - 5kHz	18	40	3.78×10^{-6}
3	5 - 10kHz	13	32	2.96×10^{-6}
4	10 - 20kHz	21	44	1.48×10^{-6}
5	20 - 30kHz	16	38	1.45×10^{-6}
6	30 - 40kHz	13	30	1.44×10^{-6}
7	40 - 50kHz	12	26	1.42×10^{-6}

where the state matrices are $\tilde{\mathbf{A}} \in \mathbb{R}^{212 \times 212}$, $\tilde{\mathbf{B}} \in \mathbb{R}^{212 \times 1}$, and $\tilde{\mathbf{C}} \in \mathbb{R}^{23 \times 212}$. Figure 2 depicts the magnitude and phase of the fitted FRF ($\tilde{\mathcal{H}}(i\omega)$) as compared to the out-of-plane component of the FRF matrix ($\mathbf{K}^{-1}(i\omega)$), derived from Eq. (5) using the SEM, for the frequency band of 30 kHz to 40 kHz. Resonant peaks and anti-resonant valleys are accurately captured by the fitted model. It should be noted that an inverse weighting scheme is adopted with the least square fit during the VF process. Thus, the VF algorithm places more importance on fitting the anti resonances than the resonant peaks. This is particularly important as the intended application of the data-driven model is to simulate the transient response of the system over the entire frequency range. The relative L_2 error, $\mathcal{E}_{L_2}^{rel}$, for individual frequency bands is provided in the Table 1 and the error for the complete frequency range is $\mathcal{E}_{L_2}^{rel} = 2.13 \times 10^{-7}$.

4.2. Transient Response Analysis and Dispersion Curves Estimation

Once the data-driven, state-space model $\tilde{\mathcal{H}}(s)$ in Eq. (12) is developed, the transient response of the structure under test can be numerically approximated by exciting $\tilde{\mathcal{H}}(s)$ with tone-burst input signals. Dispersion curves are then estimated by analyzing the waveforms propagating along the structure. Details of the this process are further presented through the following steps:

Step 1: Transient Response Simulations

The transient response of the structure under test is simulated using the developed data-driven model. An amplitude-modulated, sine wave, tone burst is selected as the excitation waveform. This waveform is selected as it is found to minimize the separation distance between the measurement location and structure's boundaries required for obtaining a reflection-free response [39]. In this study, the number of cycles is selected to be 2 when the strongly dispersive flexural waves are being considered and 1 for the weakly dispersive longitudinal waves.

The data-driven model is then used to calculate the response of the structure at all 22 points on the beam where FRFs are originally obtained. Figure 3.a shows the simulated response 10 *in.* away from the excitation point as a 2-cycle, sine wave, tone burst of a central frequency of 5 kHz is applied. As noted in the figure, due to the finite dimensions of the beam, reflections from boundaries is present in the simulated response. Structure's boundary conditions, free-free in this case, determine how the incident wave is reflected. This information is carried by the FRFs that have been used to obtain the data-driven model. Boundary condition effects on estimating dispersion curves are further discussed in Section 6.

Step 2: Incident Waveform Extraction and Processing

Once the transient response is simulated at a given location, the incident waveform is extracted. This is performed by determining the first dominant peak in the simulated response, defining a time-window

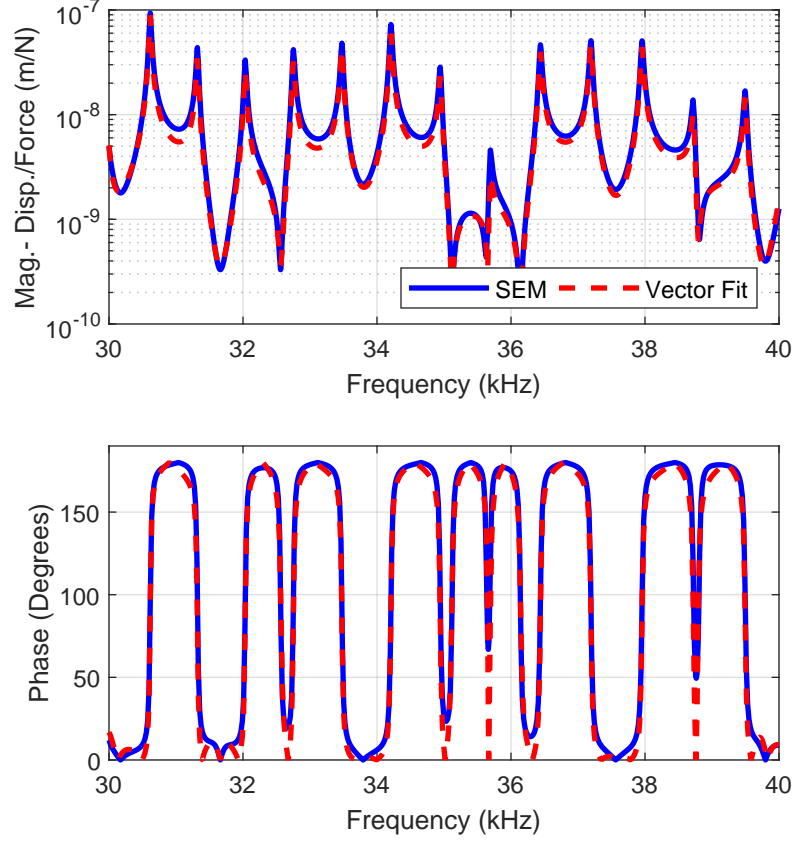


Figure 2: Out-of-plane receptance FRFs of the beam obtained by the data-driven state space model compared to the SEM predictions over the frequency range of 30 kHz to 40 kHz. FRFs are calculated 1 in. away from the excitation point.

containing the incident wave, and then applying a strongly decaying exponential functions outside that window. The size of this window is determined based on the number of cycles in the excitation signal, excitation frequency, and the location where the response is simulated. Figure 3.a shows the extracted incident wave, labeled *Processed Response* as compared to the original simulated response, 10 in. away from the excitation point. Figure 3.b shows the processed responses 2 in. and 10 in. away from the excitation point. The dispersive nature of the flexural waves at this frequency range is evident in the figure where waveform distortion and spread can be noticed as the wave propagates along the beam.

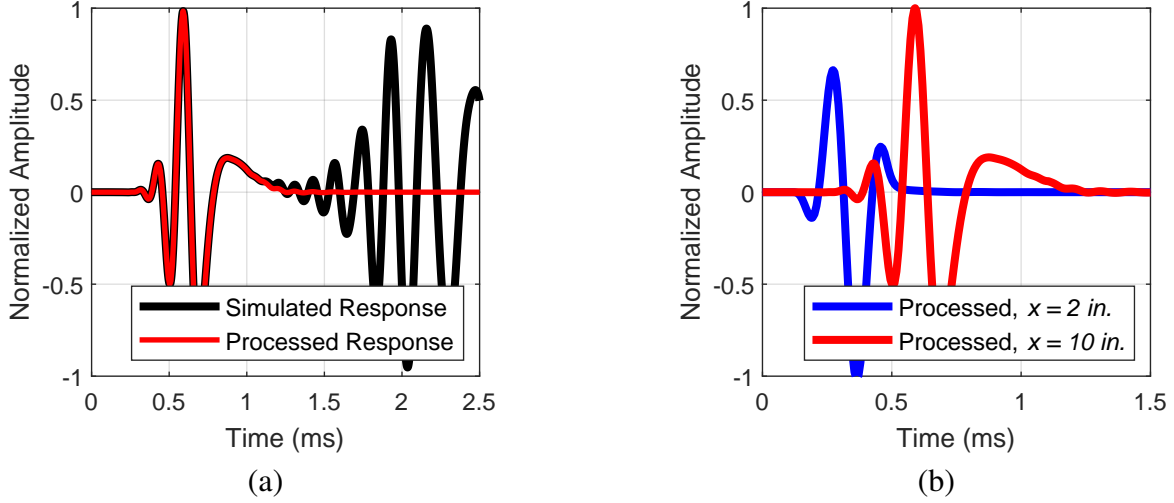


Figure 3: Flexural waveforms showing (a) simulated and processed responses 10 *in.* away from the excitation point and (b) processed responses 2 *in.* and 10 *in.* away from the excitation point. Responses are simulated with a 2-cycle sine wave tone burst excitation signal, with 5 *kHz* central frequency.

Step 3: Dispersion Curves Estimation

Given the *Processed Response* at locations i and $i + 1$, the wavenumber, k , corresponding to the wave mode under consideration can be calculated as follows

$$\mathbf{U}_{i+1}(\omega) = \mathbf{U}_i(\omega) e^{-i\mathbf{k}(x_{i+1}-x_i)}, \quad (13)$$

where \mathbf{U}_i is the vector of Fourier coefficients of the signal measured at location x_i . At the frequency range of interest, the only wave mode contributing to the out-of-plane receptance FRFs is the first anti-symmetric mode. Thus, the wavenumber vector, \mathbf{k} , only includes that wave mode. Equation (13) is solved for \mathbf{k} and the group velocity is then calculated as $V_G = \partial\omega/\partial k$. The process is then repeated where the central frequency of the excitation wave is varied to sweep the frequency range of interest. Equation (13) requires the response at two distinct points to be known. With the response being simulated at 23 points in this study, 253 different combinations can be obtained, and hence, 253 estimates of the dispersion curves can be calculated. This allows for statistical analysis to be conducted and confidence bands to be defined for the estimated dispersion curve. Such analysis is important when dealing with experimental data where noise and measurement errors can be present. Simulated responses, on the other hand, do not suffer from such sources of error, thus statistical analysis has not been included in this study.

Figure 4 depicts the group velocity of the flexural (the first anti-symmetric) wave mode calculated using the proposed data-driven modeling approach as compared to that predicted by the SEM. As depicted in the figure, the results of the data-driven modeling approach accord very well with the SEM predictions. It should be noted that at high frequency, greater than 45 *kHz*, the data-driven model fails to predict the dispersion curve. This can be ascribed to the fact that the FRFs that have been used to obtain the data-driven model over the frequency range of 0 – 50 *kHz*. Since a 2-cycle sinusoidal waveform is relatively broad-band, high-frequency signals of this form have frequency content that extends well beyond the 50 *kHz* limit of the model. Increasing the number of cycles in the excitation tone burst reduces the bandwidth of the excitation signal. This allows dispersion curves to be correctly estimated at frequencies closer to the measurement ceiling. However, the model remains limited by the frequency range over which FRFs have been obtained.

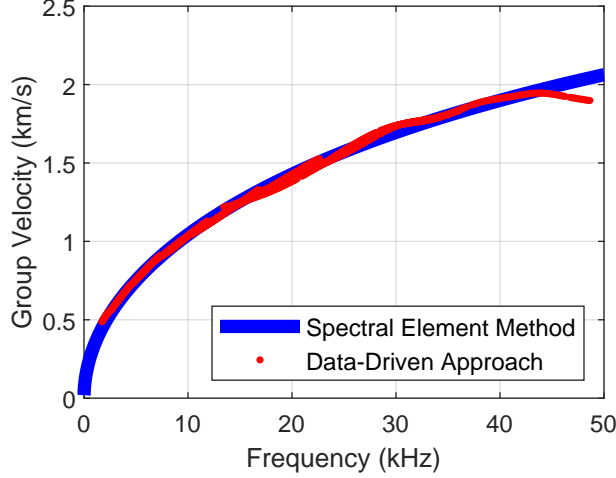


Figure 4: Comparison of group velocity curves estimated using the proposed data-driven approach (red) and that predicted by the SEM (blue) for the first anti-symmetric (flexural) wave mode.

Close examination of Figure 4 also reveals that the very low-frequency part of the dispersion curve is missing. This is due to the large wavelength of flexural waves at such low frequencies compared to the length of the beam under test. This, in turn, hinders the separation of incident and reflected waveforms, a prerequisite for Eq.(13) to be applicable. While this is an inescapable limitation for conventional wave-propagation-based experimental techniques, the use of the proposed data-driven approach allows for a number of solutions to be applied. One such solution can be to introduce artificial damping to the data-driven model in order to attenuate reflected waves. This will be the focus of future studies.

The results presented in this section highlight the capabilities of the proposed approach where a model derived from the steady-state dynamic response of the structure is employed to accurately capture its transient response and estimate its dispersion curves. The following section extends this discussion to the longitudinal wave mode.

5. Data-driven Modeling based Dispersion Curves for Longitudinal Waves

In this section, the applicability of the proposed approach to calculate the dispersion curves of the first symmetric (longitudinal) wave mode is investigated. The process presented in this section closely follows the one discussed in Section 4, the main difference is that in-plane receptance FRFs of the beam are utilized to obtain the data-driven model.

In-plane FRFs are obtained by exciting the upper and lower faces of the beam in-phase, as shown in Figure 1. Since the beam under test is perfectly symmetric with respect to its neutral axis, in-plane and out-of-plane deformation are completely uncoupled. Thus, the aforementioned excitation configuration results in pure longitudinal deformations without any contribution from flexural deformations. Figure 5 shows the transfer, longitudinal, receptance FRF, 6 – in away from the excitation location, as obtained by the SEM. As is the case for the out-of-plane deformations, the analysis is limited to the frequency range of 0 – 50 kHz.

Following the procedure outlined in Section 4.1, VF is utilized to fit the simulated longitudinal FRFs of the beam. In the frequency range of interest, the 24 resonant peaks are fitted with 48 complex-conjugate poles. The nondispersive nature of the longitudinal waves is evident from the harmonic nature of the resonant peaks. Given the relatively small number of resonant peaks in this frequency range, FRF partitioning was unnecessary in this case. Table 2 presents the order of the fitted state-space matrices and the

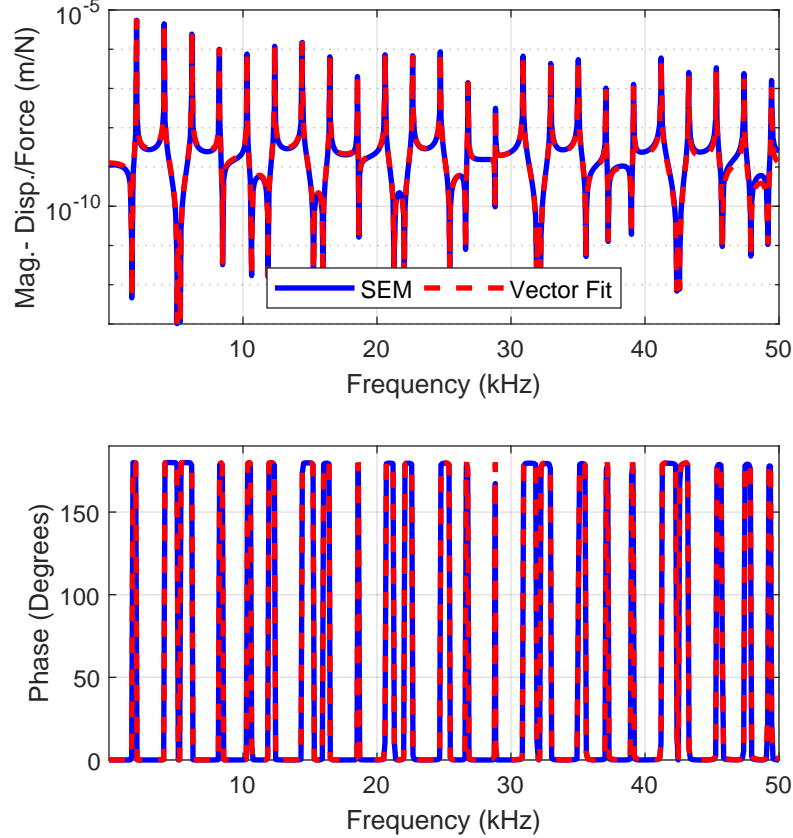


Figure 5: In-plane receptance FRF of the beam obtained by the data-driven state space model compared to the SEM predictions. FRFs are calculated 6 *in.* away from the excitation point over the frequency range of 0 – 50 *kHz*.

corresponding $\mathcal{E}_{L_2}^{rel}$ error between the fitted FRFs and the simulated ones. Additionally, the quality of the fit is illustrated by comparing the fitted FRF to the SEM prediction as shown in Figure 5.

The data-driven state-space model is then used to simulate the transient response of the system. As the longitudinal wave mode is nondispersive at this frequency range, a 1-cycle sine-wave tone burst is used as the excitation signal. Incident waveforms are then extracted from the simulated response. Figure 6.a shows the extracted incident wave, labeled *Processed Response* as compared to the original simulated response 2 *in.* away from the excitation point. Figure 6.b shows the processed responses 2 *in.* and 12 *in.* away from the excitation point. The nondispersive nature of this wave mode is seen in the figure where waveforms propagate along the beam without noticeable distortion.

While simple time-of-flight calculations can be used to estimate wave speed of nondispersive wave modes, the frequency-domain analysis presented in the previous section is followed. With the frequency-domain analysis, a given waveform can be used to estimate wave speed over a relatively wide frequency band, as opposed to a single frequency estimate with the time-of-flight calculations. Thus, statistical techniques can be implemented to define confidence intervals for the estimated dispersion curves, which is important when dealing with experimental measurements. Following Eq. (13), the processed longitudinal waveforms at locations i and $i + 1$ are analyzed and the wavenumber, k , corresponding to the first symmetric wave mode is obtained for each frequency in the excitation signal. Group velocity is then calculated and the results are shown in Figure 7. As depicted in the figure, the group velocity calculated using the data-driven approach accord very well with the SEM predictions. textcolouredAt high

Table 2: Fitting results and errors for the various data-driven models used in this study.

Boundary Conditions	State Matrices	$\mathcal{E}_{L_2}^{rel}$
Free - Free	$\tilde{\mathbf{A}} \in \mathbb{R}^{212 \times 212}$, $\tilde{\mathbf{B}} \in \mathbb{R}^{212 \times 1}$, $\tilde{\mathbf{C}} \in \mathbb{R}^{23 \times 212}$	2.13×10^{-7}
Clamped - Free	$\tilde{\mathbf{A}} \in \mathbb{R}^{214 \times 214}$, $\tilde{\mathbf{B}} \in \mathbb{R}^{214 \times 1}$, $\tilde{\mathbf{C}} \in \mathbb{R}^{16 \times 214}$	2.75×10^{-7}
Pinned - Pinned	$\tilde{\mathbf{A}} \in \mathbb{R}^{212 \times 212}$, $\tilde{\mathbf{B}} \in \mathbb{R}^{212 \times 1}$, $\tilde{\mathbf{C}} \in \mathbb{R}^{16 \times 212}$	3.09×10^{-7}
Free - Free (inplane)	$\tilde{\mathbf{A}} \in \mathbb{R}^{48 \times 48}$, $\tilde{\mathbf{B}} \in \mathbb{R}^{48 \times 1}$, $\tilde{\mathbf{C}} \in \mathbb{R}^{23 \times 48}$	3.12×10^{-7}

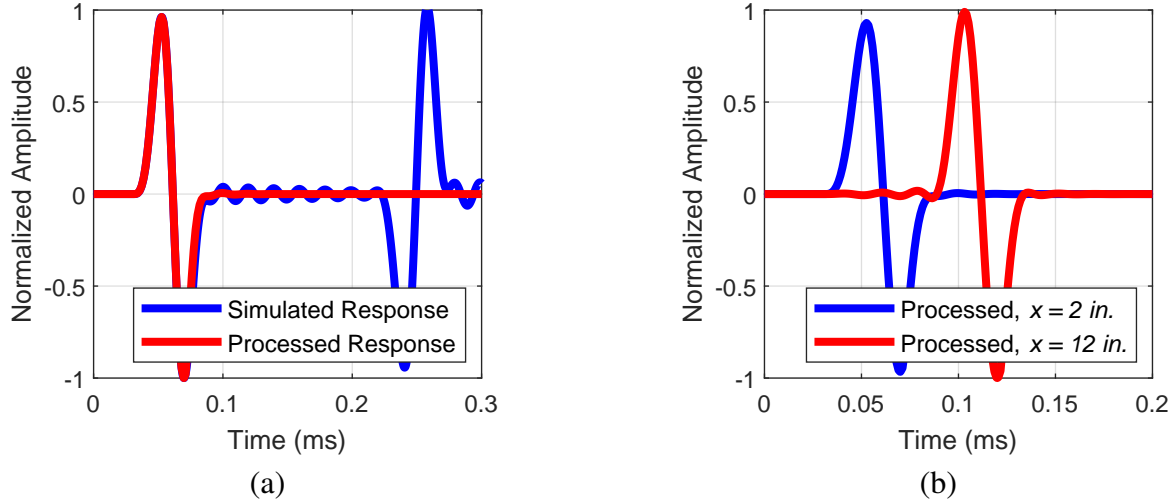


Figure 6: Longitudinal waveforms showing (a) simulated and processed responses 2 in. away from the excitation point, and (b) processed responses 2 in. and 12 in. away from the excitation point. Responses are simulated with a 1-cycle sine wave tone burst excitation signal, with 20 kHz central frequency.

frequency, > 40 kHz, the proposed approach fails to predict the dispersion curve. This is due to the broadband nature of the 1-cycle tone bursts and the limited frequency range over which FRFs are obtained. The very low-frequency part of the dispersion curve is also missing since the large wavelength of longitudinal waves at such low frequencies hinders the separation of incident and reflected waveforms.

6. On the Effects of Boundary Conditions

In this section, the effects of boundary conditions on the performance of the proposed approach are investigated. While end conditions do not affect wave propagation characteristics along the waveguide, they determine how waves are reflected at the boundaries, which has a profound impact on measured FRFs. The goal of this section is to demonstrate that such changes in FRFs will not affect dispersion curves estimates. For this purpose, two additional combinations of boundary conditions are investigated, these are clamped-free and pinned-pinned conditions. out-of-plane receptance FRFs for these boundary conditions are obtained using the SEM. The VF algorithm is then used to create a data-driven, SIMO model for each set of boundary conditions. Table 2 summarizes fitting results for these boundary conditions, along with the free-free conditions discussed in the previous sections. The dimensions of the state matrices and the relative fit error for each case are given in the table. Figure 8 depicts out-of-plane re-

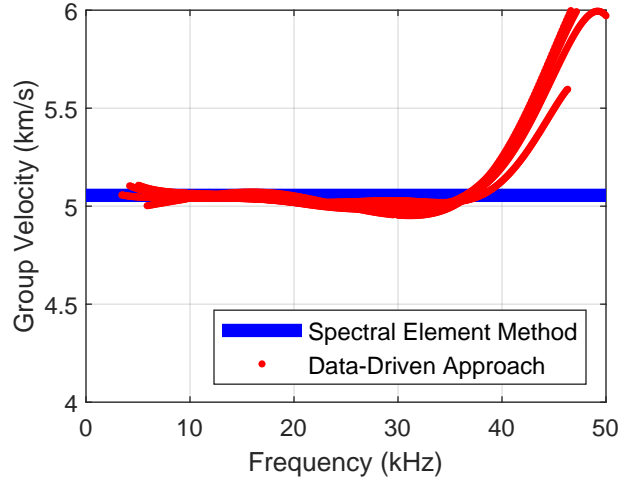


Figure 7: Comparison of group velocity curves estimated using the proposed data-driven approach (red) and that predicted by the SEM (blue) for the first symmetric (longitudinal) wave mode.

ceptance FRFs of the beam with clamped-free and pinned-pinned boundary conditions, where simulated and fitted FRFs are compared. The impact of boundary conditions on FRFs is evident.

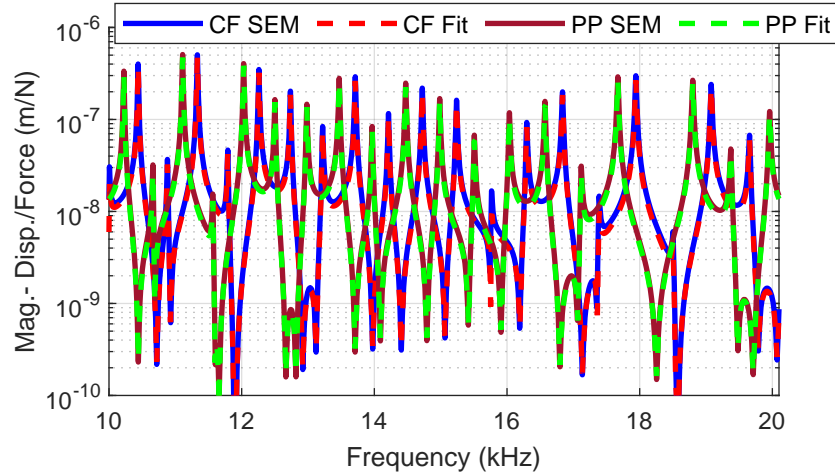


Figure 8: Out-of-plane receptance FRFs of the beam with clamped-free and pinned-pinned boundaries over the frequency range of 10 kHz to 20 kHz. Simulated and fitted FRFs are compared. FRFs are calculated 1 in. away from the excitation point.

Following the procedure outlined in Section 4, dispersion curves are estimated using the clamped-free, and the pinned-pinned, data-driven models. The results are summarized in Figure 9. Although the FRFs used to obtain the data-driven models are affected by changes in boundary conditions, such effects are not reflected on the estimated dispersion curves. Both clamped-free and pinned-pinned models are capable of accurately estimating dispersion curves, as suggested by the figure. It should be noted that the previously discussed limitations at the upper- and lower-ends of the frequency range are applicable to the current cases. While the analysis presented in this section is limited to flexural deformations, the conclusions are equally valid for longitudinal deformations. Observations based on the numerical experiments presented in this section highlight the capability of the approach in dealing with various boundary conditions. In future studies, the robustness of the proposed approach to uncertainties and noise in the experimental data of structures under real-boundary conditions will be investigated.

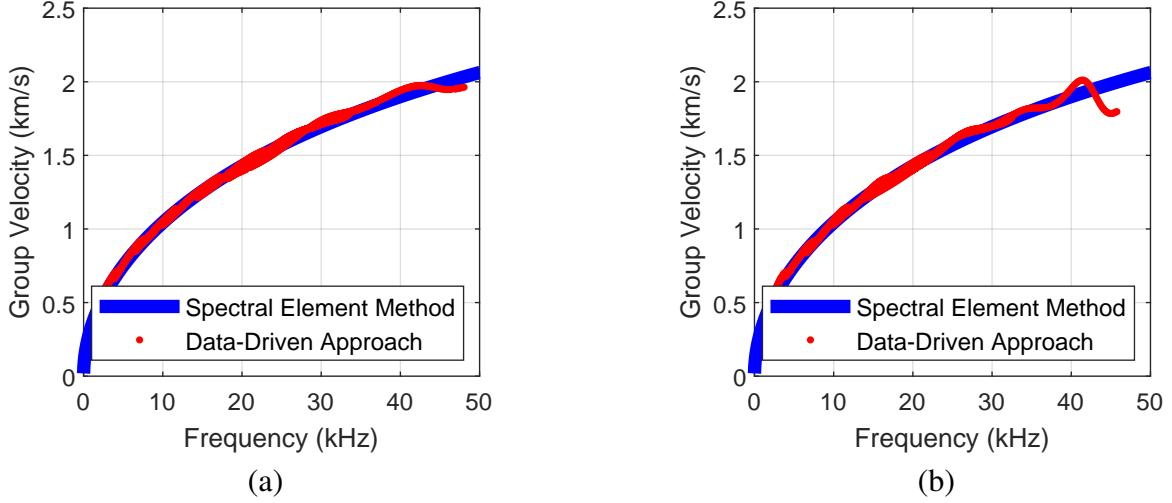


Figure 9: Group velocity curves for the first anti-symmetric wave mode estimated using (a) fixed-free, and (b) pinned-pinned data-driven models.

7. Conclusions

In this paper, a new data-driven modeling approach for estimating dispersion curves is presented. The Vector Fitting method is adopted to develop a single-input-multi-output, state-space, dynamical model of the beam under test based on receptance FRFs. FRFs corresponding to longitudinal and lateral deformations of the beam are simulated over the frequency range of 0 – 50 kHz. The data-driven model is able to accurately capture the dynamic behaviour of the system within the frequency range of interest with an error of $\mathcal{E}_{L_2}^{rel} = 2.13 \times 10^{-7}$ for lateral deformations, and $\mathcal{E}_{L_2}^{rel} = 3.12 \times 10^{-7}$ for longitudinal deformations.

The data driven model is then used to study wave propagation along the beam and obtain its dispersion curves. Group velocity curves corresponding to symmetric and anti-symmetric wave modes are estimated with this approach over the frequency range of 2 – 40 kHz. The results are found to be in very good agreement with the numerical predictions of the SEM. Dispersion curves at frequencies lower than 2 kHz cannot be estimated directly using this approach. This is due to the large wavelength at such low frequencies compared to the length of the beam under test, which hinders the separation of incident and reflected waveforms. While this is a limitation of all current experimental practices, the proposed approach allows for potential solutions to be implemented, such as the introduction of artificial damping to attenuate reflected waves, which will be addressed in future studies.

The effects of boundary conditions on the performance of the developed approach have also been studied in this work. Although boundary conditions have a profound impact on the FRFs that are used for the data-driven models, estimated group velocity curves are found to be unaffected by such conditions. This allows for this approach to be used regardless of boundary conditions of the structure under test, which is crucial for many practical applications.

The work presented herein demonstrates the feasibility of estimating dispersion curves based on steady-state FRFs using this new data-driven modeling approach. The experimental implementation of this technique will be investigated in future studies, where the issues of model order selection, parameter identification, and the introduction of artificial damping will be investigated. Future studies will also address the scenarios where different wave modes are coupled or simultaneously excited where the impact of coupling at the FRF-level on predicted dispersion curves will be investigated.

Acknowledgment

Tarazaga would like to acknowledge the support provided by the John R. Jones III Faculty Fellowship. The work of Gugercin was supported in parts by NSF through Grant DMS-1522616 and DMS-1720257. The work of Albakri was supported in parts by the Federal Railroad Administration.

Appendix A: Spectral Element Matrices

For a two-node spectral finite element, vectors \mathbf{d} and \mathbf{F} in Eq. 5 as defined as follows

$$\mathbf{d} = \left\{ U_0(x_1) \quad W_0(x_1) \quad \Phi(x_1) \quad U_0(x_2) \quad W_0(x_2) \quad \Phi(x_2) \right\}^T,$$

$$\mathbf{F} = \left\{ -\bar{F}_x(x_1) \quad -\bar{F}_z(x_1) \quad -\bar{M}(x_1) \quad \bar{F}_x(x_2) \quad \bar{F}_z(x_2) \quad \bar{M}(x_2) \right\}^T,$$

where U_0 , W_0 , Φ , \bar{F}_x , \bar{F}_z , and \bar{M} are, respectively, the longitudinal displacement, the lateral displacement of the beam's neutral axis, the angle of rotation of the neutral axis normal vector, the externally applied axial force, lateral force, and bending moments in the frequency domain. x_1 and x_2 are the coordinates of the left and right nodes of the spectral finite element.

The shape functions matrix, $\Psi(i\omega)$, in Eq. 5, is defined for a two-node spectral finite element as follows

$$\Psi(i\omega) = \begin{bmatrix} \zeta_{11} & \zeta_{21} & 0 & 0 & 0 & 0 \\ 0 & 0 & \zeta_{31} & \zeta_{41} & \zeta_{51} & \zeta_{61} \\ 0 & 0 & r_{33}\zeta_{31} & r_{34}\zeta_{41} & r_{35}\zeta_{51} & r_{36}\zeta_{61} \\ \zeta_{12} & \zeta_{22} & 0 & 0 & 0 & 0 \\ 0 & 0 & \zeta_{32} & \zeta_{42} & \zeta_{52} & \zeta_{62} \\ 0 & 0 & r_{33}\zeta_{32} & r_{34}\zeta_{42} & r_{35}\zeta_{52} & r_{36}\zeta_{62} \end{bmatrix},$$

where $\zeta_{mj} = e^{-ik_m(i\omega)x_j}$ with $m = 1, 2, \dots, 6$, and $j = 1, 2$.

The non-zero elements of the boundary conditions matrix, $G(i\omega)$ are

$$\begin{aligned} G_{1s} &= ik_{sn}EAe^{-ik_{sn}x_1} \\ G_{2t} &= GA\bar{K}(-ik_{tn} + r_{3t})e^{-ik_{tn}x_1} \\ G_{3t} &= -iEI k_{tn}e^{-ik_{tn}x_1} \\ G_{4s} &= ik_{msn}EAe^{-ik_{sn}x_2} \\ G_{5t} &= GA\bar{K}(-ik_{tn} + r_{3t})e^{-ik_{tn}x_2} \\ G_{6t} &= -iEI k_{tn}e^{-ik_{tn}x_2} \end{aligned}$$

where $s = 1, 2$ and $t = 3, 4, 5, 6$.

References

- [1] M. I. Albakri, V. S. Malladi, P. A. Tarazaga, Low-frequency acoustoelastic-based stress state characterization: Theory and experimental validation, *Mechanical Systems and Signal Processing* 112 (2018) 417–429.

- [2] J. Schloemann, V. V. N. S. Malladi, A. G. Woolard, J. M. Hamilton, R. M. Buehrer, P. A. Tarazaga, Vibration event localization in an instrumented building, in: *Experimental Techniques, Rotating Machinery, and Acoustics*, Volume 8, Springer, 2015, pp. 265–271.
- [3] J. D. Poston, J. Schloemann, R. M. Buehrer, V. V. N. S. Malladi, A. G. Woolard, P. A. Tarazaga, Towards indoor localization of pedestrians via smart building vibration sensing, in: *Localization and GNSS (ICL-GNSS)*, 2015 International Conference on, IEEE, 2015, pp. 1–6.
- [4] A. G. Woolard, P. A. Tarazaga, Applications of dispersion compensation for indoor vibration event localization, *Journal of Vibration and Control* (2017) 1077546317744997.
- [5] C. Caloz, Metamaterial dispersion engineering concepts and applications, *Proceedings of the IEEE* 99 (10) (2011) 1711–1719.
- [6] K. F. Graff, *Wave motion in elastic solids*, Courier Corporation, 2012.
- [7] A. Chaigne, Structural acoustics and vibrations, in: *Springer Handbook of Acoustics*, Springer, 2014, pp. 941–1000.
- [8] G.-R. Liu, Z. Xi, *Elastic waves in anisotropic laminates*, CRC press, 2001.
- [9] J. F. Doyle, *Wave propagation in structures: spectral analysis using fast discrete Fourier transforms*, Springer, 1997.
- [10] S. Gopalakrishnan, A. Chakraborty, D. R. Mahapatra, *Spectral finite element method: wave propagation, diagnostics and control in anisotropic and inhomogeneous structures*, Springer Science & Business Media, 2007.
- [11] U. Lee, *Spectral element method in structural dynamics*, John Wiley & Sons, 2009.
- [12] M. Palacz, Spectral methods for modelling of wave propagation in structures in terms of damage detection: a review, *Applied Sciences* 8 (7) (2018) 1124.
- [13] A. Marzani, E. Viola, I. Bartoli, F. L. Di Scalea, P. Rizzo, A semi-analytical finite element formulation for modeling stress wave propagation in axisymmetric damped waveguides, *Journal of Sound and Vibration* 318 (3) (2008) 488–505.
- [14] R. Joseph, L. Li, M. F. Haider, V. Giurgiutiu, Hybrid safe-gmm approach for predictive modeling of guided wave propagation in layered media, *Engineering Structures* 193 (2019) 194–206.
- [15] B. R. Mace, E. Manconi, Modelling wave propagation in two-dimensional structures using finite element analysis, *Journal of Sound and Vibration* 318 (4-5) (2008) 884–902.
- [16] C. Zhou, J. Lainé, M. Ichchou, A. Zine, Wave finite element method based on reduced model for one-dimensional periodic structures, *International Journal of Applied Mechanics* 7 (02) (2015) 1550018.
- [17] H. Al Ba’ba’a, M. Nouh, T. Singh, Formation of local resonance band gaps in finite acoustic metamaterials: A closed-form transfer function model, *Journal of Sound and Vibration* 410 (2017) 429–446.

- [18] F. Li, C. Zhang, C. Liu, Active tuning of vibration and wave propagation in elastic beams with periodically placed piezoelectric actuator/sensor pairs, *Journal of Sound and Vibration* 393 (2017) 14–29.
- [19] S. Bilbao, *Wave and scattering methods for numerical simulation*, John Wiley & Sons, 2004.
- [20] B. D. O. Anderson, A. C. Antoulas, Rational interpolation and state variable realization, *Linear Algebra and Its Applications*, Special Issue on Matrix Problems 137/138 (1990) 479–509.
- [21] A. C. Antoulas, S. Lefteriu, A. C. Ionita, A tutorial introduction to the Loewner framework for model reduction, in: *Model Reduction and Approximation*, SIAM, Philadelphia, 2017, pp. 335–376.
- [22] A. Mayo, A. Antoulas, A framework for the solution of the generalized realization problem, *Linear Algebra and Its Applications* 425 (2-3) (2007) 634–662.
- [23] P. Schulze, B. Unger, C. Beattie, S. Gugercin, Data-driven structured realization, *Linear Algebra and its Applications* 537 (2018) 250–286.
- [24] J. M. Hokanson, Projected nonlinear least squares for exponential fitting, *SIAM Journal on Scientific Computing* 39 (6) (2017) A3107–A3128.
- [25] P. Gonnet, R. Pachón, L. N. Trefethen, Robust rational interpolation and least-squares, *Electronic Transactions on Numerical Analysis* 38 (2011) 146–167.
- [26] B. Gustavsen, A. Semlyen, Rational approximation of frequency domain responses by vector fitting, *IEEE Transactions on power delivery* 14 (3) (1999) 1052–1061.
- [27] Z. Drmač, S. Gugercin, C. Beattie, Quadrature-based vector fitting for discretized \mathcal{H}_2 approximation, *SIAM J. Sci. Comp.* 37 (2) (2015) A625–A652.
- [28] M. Berljafa, S. Güttel, The RKFIT algorithm for nonlinear rational approximation, *SIAM Journal on Scientific Computing* 39 (5) (2017) 2049–2071.
- [29] Y. Nakatsukasa, O. Sète, L. N. Trefethen, The AAA algorithm for rational approximation, *SIAM Journal on Scientific Computing* 40 (3) (2018) A1494–A1522.
- [30] Y. Nakatsukasa, L. N. Trefethen, An algorithm for real and complex rational minimax approximation, *arXiv preprint arXiv:1908.06001*.
- [31] V. V. S. Malladi, M. I. Albakri, P. A. Tarazaga, S. Gugercin, Data-driven modeling techniques to estimate dispersion relations of structural components, in: *ASME 2018 Conference on Smart Materials, Adaptive Structures and Intelligent Systems*, American Society of Mechanical Engineers, 2018, pp. V001T03A026–V001T03A026.
- [32] U. Lee, D. Kim, I. Park, Dynamic modeling and analysis of the pzt-bonded composite timoshenko beams: spectral element method, *Journal of Sound and Vibration* 332 (6) (2013) 1585–1609.
- [33] M. I. Albakri, P. A. Tarazaga, Dynamic analysis of a piezoelectric augmented beam system with adhesive bonding layer effects, *Journal of Intelligent Material Systems and Structures* 28 (2) (2017) 178–194.

- [34] Z. Drmač, S. Gugercin, C. Beattie, Vector fitting for matrix-valued rational approximation, *SIAM Journal on Scientific Computing* 37 (5) (2015) A2346–A2379.
- [35] C. Sanathanan, J. Koerner, Transfer function synthesis as a ratio of two complex polynomials, *IEEE Trans. Autom. Control* 8 (1) (1963) 56–58.
- [36] Z. Drmac, S. Gugercin, C. Beattie, Quadrature-based vector fitting for discretized h₂ approximation, *SIAM Journal on Scientific Computing* 37 (2) (2015) A625–A652.
- [37] B. Gustavsen, Improving the pole relocating properties of vector fitting, *IEEE Transactions on Power Delivery* 21 (3) (2006) 1587–1592.
- [38] A. Chinae, S. Grivet-Talocia, On the parallelization of Vector Fitting algorithms, *IEEE Transactions on Components, Packaging and Manufacturing Technology* 1 (11) (2011) 1761–1773.
- [39] M. I. Albakri, P. A. Tarazaga, A novel acoustoelastic-based technique for stress measurement in structural components, in: *Dynamics of Civil Structures*, Volume 2, Springer, 2016, pp. 49–56.